

# Supporting Information

## Charge-Transfer Plasmon Polaritons at Graphene/ $\alpha$ -RuCl<sub>3</sub> Interfaces

Daniel J. Rizzo<sup>1</sup>, Bjarke S. Jessen<sup>1,2</sup>, Zhiyuan Sun<sup>1</sup>, Francesco L. Ruta<sup>1,3</sup>, Jin Zhang<sup>4</sup>, Jia-Qiang Yan<sup>5,6</sup>, Lede Xian<sup>4</sup>, Alexander S. McLeod<sup>1</sup>, Michael E. Berkowitz<sup>1</sup>, Kenji Watanabe<sup>7</sup>, Takashi Taniguchi<sup>8</sup>, Stephen E. Nagler<sup>9</sup>, David G. Mandrus<sup>5,6</sup>, Angel Rubio<sup>4,10,11</sup>, Michael M. Fogler<sup>12</sup>, Andrew J. Millis<sup>1,10</sup>, James C. Hone<sup>2</sup>, Cory R. Dean<sup>1</sup>, D.N. Basov<sup>1,\*</sup>

<sup>1</sup>Department of Physics, Columbia University, New York, New York 10027, United States

<sup>2</sup>Department of Mechanical Engineering, Columbia University, New York, New York 10027, United States

<sup>3</sup>Department of Applied Physics and Applied Mathematics, Columbia University, New York, New York 10027, United States

<sup>4</sup>Theory Department, Max Planck Institute for Structure and Dynamics of Matter and Center for Free-Electron Laser Science, 22761 Hamburg, Germany

<sup>5</sup>Materials Science and Technology Division, Oak Ridge National Laboratory, Oak Ridge, Tennessee 37831, United States

<sup>6</sup>Department of Materials Science and Engineering, University of Tennessee, Knoxville, Tennessee 37996, United States

<sup>7</sup>Research Center for Functional Materials, National Institute for Materials Science, 1-1 Namiki, Tsukuba 305-0044, Japan

<sup>8</sup>International Center for Materials Nanoarchitectonics, National Institute for Materials Science, 1-1 Namiki, Tsukuba 305-004, Japan

<sup>9</sup>Neutron Scattering Division, Oak Ridge National Laboratory, Oak Ridge, Tennessee 37831, United States

<sup>10</sup>Center for Computational Quantum Physics, Flatiron Institute, New York, New York 10010, United States

<sup>11</sup>Nano-Bio Spectroscopy Group, Universidad del País Vasco UPV/EHU, San Sebastián 20018, Spain

<sup>12</sup>Department of Physics, University of California San Diego, La Jolla, California 92093, United States

\*Email: db3056@columbia.edu .

## Table of Contents

<b>Supplementary Discussion</b>	3
S1. Fitting Calculated Plasmon Dispersions to the Experimental Data	3
I. Modeling the surface and edge CPP dispersions	3
II. Least-squares optimization of the chemical potential	7
S2. Characterizing the graphene/ $\alpha$ -RuCl <sub>3</sub> interfacial optical response from the CPP losses	8
I. Graphene phonon contribution to the plasmon scattering rate	9
II. Extracted optical conductivity of doped $\alpha$ -RuCl <sub>3</sub>	10
S3. Modeling near-field signal from plasmon reflection at a point defect	11
S4. Ab Initio Calculations of Graphene/ $\alpha$ -RuCl <sub>3</sub> Heterostructures	12
<b>Figure S1.</b> Schematic of assembly for <i>h</i> BN/graphene/ $\alpha$ -RuCl <sub>3</sub> /SiO <sub>2</sub> /Si	14
<b>Figure S2.</b> Theoretical electronic structure of freestanding $\alpha$ -RuCl <sub>3</sub> and graphene/ $\alpha$ -RuCl <sub>3</sub> with <i>h</i> BN spacers.	15
<b>Figure S3:</b> Comparison of Near-field Amplitude of <i>h</i> BN/graphene/ $\alpha$ -RuCl <sub>3</sub> /SiO <sub>2</sub> vs. <i>h</i> BN/graphene/SiO <sub>2</sub>	16
<b>Figure S4.</b> Examples fits to the three types of CPP cross-sections.	17
<b>Figure S5.</b> Model CPP dispersions of <i>h</i> BN/graphene/ $\alpha$ -RuCl <sub>3</sub> /SiO <sub>2</sub> with and without doped interfacial $\alpha$ -RuCl <sub>3</sub>	18
<b>Figure S6.</b> Analysis of circular CPP fringes near point defects in graphene/ $\alpha$ -RuCl <sub>3</sub> heterostructures.	19
<b>Figure S7.</b> Raman analysis of <i>h</i> BN/graphene/ $\alpha$ -RuCl <sub>3</sub> /SiO <sub>2</sub>	20
<b>Figure S8.</b> Schematic of the <i>h</i> BN/graphene/ $\alpha$ -RuCl <sub>3</sub> /SiO <sub>2</sub> /Si heterostructure.	21
<b>Figure S9.</b> Temperature-dependent scattering in graphene/ $\alpha$ -RuCl <sub>3</sub>	22
<b>References</b>	23

## Supplementary Discussion

### S1. Fitting Calculated Plasmon Dispersions to the Experimental Data

#### I. Modeling the surface and edge CPP dispersions

In this section we discuss our analytical formalism for modeling the CPP excitations in our experimental device. The system geometry adopted in the model is shown schematically in Figure S8. We treated graphene as a 2D Drude metal of negligible thickness and sheet conductivity

$$\sigma_g(\omega) = \frac{i}{\pi} \frac{D_g}{\omega + i\gamma_g(\omega)}, \quad (\text{S1})$$

where  $\gamma_g$  is the frequency-dependent damping rate discussed in the main text and section S2 and  $D_g = (e^2/\hbar^2)|\mu|$  is the Drude weight proportional to the graphene chemical potential  $\mu$ . The carrier density in graphene satisfies the equation  $|n| = (|\mu|/\hbar v_F)^2/\pi$ , where  $v_F = 10^8 \text{ cm s}^{-1}$  is the graphene Fermi velocity. We refer to the *h*BN layer above the graphene plus the vacuum beyond it as the graphene superstrate. We refer to the stack of layers below graphene as the graphene substrate. In our model, the substrate consists of a doped  $\alpha$ -RuCl<sub>3</sub> layer, an undoped  $\alpha$ -RuCl<sub>3</sub>, and an SiO<sub>2</sub> layer.

We indexed all the layers in the super- and substrate consecutively from top to bottom by integer  $j = 0, \dots, 4$  and denoted their thicknesses by  $d_j$ . Thicknesses  $d_0$  and  $d_4$  are set to be infinite. The numerical values of *h*BN thickness  $d_1 = 2.9 \text{ nm}$  and the total  $\alpha$ -RuCl<sub>3</sub> thickness  $d_2 + d_3 = 2.5 \text{ nm}$  were inferred from atomic force microscopy (AFM). The discontinuous change in doping of  $\alpha$ -RuCl<sub>3</sub> is a simplifying assumption; in fact, the doping level should vary gradually. To model the doping of only the interfacial layers as suggested by the DFT, we set  $d_3 = 1.9 \text{ nm}$ . In the first approximation, the doped  $\alpha$ -RuCl<sub>3</sub> layer and graphene act as a single 2D system with a certain total sheet conductivity  $\sigma = \sigma_g + \sigma_s$ .

To take advantage of the approach developed in a previous work<sup>1</sup> and also for greater generality, we modeled each layer as a uniaxial dielectric with an in-plane permittivity  $\epsilon_j^\perp(\omega)$  and an out-of-plane permittivity  $\epsilon_j^\parallel(\omega)$ . The geometric average of these quantities is denoted by  $\epsilon_j \equiv (\epsilon_j^\perp)^{1/2} (\epsilon_j^\parallel)^{1/2}$ . In the actual calculation, only the *h*BN layer was treated as uniaxial. The permittivity of all the other layers was taken to be isotropic,  $\epsilon_j^\perp = \epsilon_j^\parallel = \epsilon_j$ . This simplifying assumption may be a source of some inaccuracy because  $\alpha$ -RuCl<sub>3</sub> is monoclinic at room temperature. Finally, we described the effect of doping on  $\alpha$ -RuCl<sub>3</sub> by another phenomenological correction of Drude type:

$$\epsilon_2^a(\omega) - \epsilon_3^a(\omega) = -\frac{(v^a)^2}{\omega(\omega + i\gamma_s)}, \quad a = \perp \text{ or } z, \quad (\text{S3})$$

where  $v^a$  and  $\gamma_s$  are adjustable parameters. As mentioned above, if  $d_2$  is small, it is permissible to lump layer 2 with graphene by converting the in-plane correction  $\epsilon_2^\perp(\omega) - \epsilon_3^\perp(\omega)$  into the correction to graphene sheet conductivity:

$$\sigma_s(\omega) = \frac{i}{\pi} \frac{D_s}{\omega + i\gamma_s(\omega)}, \quad D_s = \frac{1}{4}(v^\perp)^2 d_2. \quad (\text{S4})$$

(Conversely, if  $\sigma_s$  and  $d_2$  are considered primary parameters, one can use these equations to obtain  $\epsilon_2^\perp - \epsilon_3^\perp$ ). Assuming the 2D carrier density in the doped  $\alpha$ -RuCl<sub>3</sub> layer is equal in magnitude and opposite in sign to that in graphene, we can estimate the corresponding 2D Drude weight by  $D_s =$

$\pi|n|e^2/m^*$  where the lower bound of the effective mass of carriers  $m^*$  is provided by the DFT. The scattering rate  $\gamma_s(\omega)$  is discussed in more detail in Section S2 below.

The influence of the substrate and the superstrate on electrodynamics of charge carriers in graphene can be described by frequency and momentum dependent permittivities,  $\kappa_{\text{sub}} = \kappa_{\text{sub}}(\omega, q)$  and  $\kappa_{\text{sup}} = \kappa_{\text{sup}}(\omega, q)$ . In the quasi-static limit  $q \gg \omega/c$ , which is relevant for our near-field experiment, we can compute these quantities from the formula

$$\kappa_s = (1 + r_{P_s})/(1 - r_{P_s}), \quad s = \text{sub or sup.} \quad (\text{S5})$$

This equation derives from the quasi-static approximation for the  $P$ -polarization Fresnel reflection coefficient of  $j, j + 1$  interface:  $r_{j,j+1} \simeq (\epsilon_{j+1} - \epsilon_j)/(\epsilon_{j+1} + \epsilon_j)$ . Specifically, Eq. (S5) can be derived once the replacements  $r_{j,j+1} \rightarrow r_{P_s}$ ,  $\epsilon_{j+1} \rightarrow \kappa_s$ , and  $\epsilon_j \rightarrow \epsilon_0 = 1$  are made. Here  $r_{P_s}$  is the reflection coefficient of the stack  $s$ . To compute such  $r_{P_s}$  we used the recursion method of<sup>1</sup>. For the case of substrate, it is applied as follows. The base of the recursion is a partial reflection coefficient  $r_{M-1} \equiv r_{M-1,M}$  where  $M = 4$  is the index of the bottom substrate layer, i.e., the layer farthest from graphene. At each recursion step, another partial reflection coefficient  $r_j$  is computed, for  $j$  lowered by one, (that is, for one position closer to graphene). The net reflection coefficient  $r_{P_{\text{sub}}}$  is given by  $r_{P_{\text{sub}}} = r_N$  where  $N = 1$  is the index of the substrate layer next to graphene. In the cited reference<sup>1</sup>, a more general model was considered where interfaces between adjacent layers  $j, j + 1$  were assumed to have some sheet conductivities  $\sigma_{j,j+1}$ , in which case the full set of equations employed in the calculation is

$$\begin{aligned} r_j &= r_{j,j+1} - \frac{(1 - r_{j,j+1})(1 - r_{j+1,j})r_{j+1}}{r_{j+1,j}r_{j+1} - \exp(-2ik_{j+1}^z d_{j+1})}, \\ r_{j,j+1} &= \frac{Q_{j+1} - Q_j + \frac{4\pi}{\omega} \sigma_{j,j+1}}{Q_{j+1} + Q_j + \frac{4\pi}{\omega} \sigma_{j,j+1}}, \\ Q_j &= \frac{\epsilon_j^\perp}{k_j^z}, \quad k_j^z = \sqrt{\epsilon_j^\perp} \sqrt{\frac{\omega^2}{c^2} - \frac{q^2}{\epsilon_j^\parallel}}. \end{aligned} \quad (\text{S6})$$

In the generic case  $d_2 > 0$ , only  $\sigma_{12} = \sigma_g$  is nonzero and actually it does not enter the calculation of  $r_{P_{\text{sub}}}$  because the recursion terminates at  $j = 1$ . However, by continuing through to  $j = 0$ , we can obtain the reflection coefficient  $r_P$  of the entire heterostructure (the top encapsulating layer plus graphene plus the substrate stack). To compute the reflection coefficient  $r_{P_{\text{sup}}}$  of the superstrate, we followed the same scheme as for  $r_{P_{\text{sub}}}$  except with the layer order inverted, i.e., we always run the recursion from the layer farthest from graphene to the one closest to it. It is easy to derive a closed-form expression for  $\kappa_{\text{sup}}$ :

$$\kappa_{\text{sup}} = \epsilon_1 \frac{\epsilon_0 + \epsilon_1 \tanh(-ik_1^\parallel d_1)}{\epsilon_1 + \epsilon_0 \tanh(-ik_1^\parallel d_1)}, \quad k_1^\parallel = i \frac{\sqrt{\epsilon_1^\perp}}{\sqrt{\epsilon_1^\parallel}} q. \quad (\text{S7})$$

The net effective permittivity of the graphene environment is equal to the average of the substrate and superstrate permittivities:

$$\kappa(\omega, q) = (\kappa_{\text{sub}} + \kappa_{\text{sup}})/2 = \kappa_1 + i\kappa_2. \quad (\text{S8})$$

The momentum dependence of function  $\kappa(\omega, q)$  can be understood from the following qualitative argument. The electric field created by charges in graphene spreads over the vertical

distance that scales as  $1/q$ . Therefore, at large  $q$ , the field is strongly confined in the layers  $j = 1$  and  $j = 2$  adjacent to graphene, so that  $\kappa$  should approach the average of their permittivities:

$$\kappa(\omega, \infty) = (\epsilon_1 + \epsilon_2)/2. \quad (\text{S9})$$

Conversely, at small  $q$ , the electric field penetrates far beyond the adjacent layers and resides mainly in the semi-infinite  $j = 0$  and  $j = 4$  strata (vacuum and SiO<sub>2</sub>), so that  $\kappa \approx (\epsilon_0 + \epsilon_4)/2$ . At intermediate momenta, the function  $\kappa$  should smoothly interpolate between these limiting values.

Once  $\kappa$  is known, we can compute the effective 2D dielectric function of graphene. It has a well-known form

$$\epsilon(\omega, q) = 1 - \frac{1}{\kappa(\omega, q)} \frac{q}{q_p(\omega)}, \quad q_p(\omega) \equiv \frac{i\omega}{2\pi\sigma_g(\omega)} = \frac{\omega(\omega + i\gamma)}{2D_g}, \quad (\text{S10})$$

where  $q_p(\omega)$  has the physical meaning of the CPP momentum of graphene suspended in vacuum,  $\kappa = 1$ .

To handle  $d_2 \rightarrow 0$  limit, it is natural to introduce two obvious changes into this general scheme. The first one is to replace  $\sigma_g$  in Eq. (S10) by  $\sigma_g + \sigma_s$ . The second one is to redefine the substrate as layers  $j = 3$  plus 4 only. The corresponding  $\kappa_{\text{sub}}$  is given by [cf. Eq. (S7)]

$$\kappa_{\text{sub}} = \epsilon_3 \frac{\epsilon_4 + \epsilon_3 \tanh(-ik_3^{\parallel} d_3)}{\epsilon_3 + \epsilon_4 \tanh(-ik_3^{\parallel} d_3)}, \quad k_3^{\parallel} = i \frac{\sqrt{\epsilon_3^{\perp}}}{\sqrt{\epsilon_3^{\parallel}}} q. \quad (\text{S11})$$

In this reformulation,  $\kappa_{\text{sub}} \rightarrow \epsilon_3$  as  $q \rightarrow \infty$ .

To compute the dispersions of the CPPs and edge CPPs we analyzed the behavior of the dielectric function  $\epsilon(\omega, q)$ . For the CPP, our procedure was as follows. The complex CPP momentum  $q_s = q_1 + iq_2$  is the root of  $\epsilon(\omega, q)$  for a given real  $\omega$ , which, per Eq. (S9), is the solution of the equation

$$q_s = q_p(\omega)\kappa(\omega, q). \quad (\text{S10})$$

To find the real part  $q_1 = \text{Re } q_s$  of this solution we employed an approximation that  $q_1(\omega)$  coincides with the maximum of the loss function of graphene

$$f(\omega, q) \equiv -\text{Im} \frac{1}{\epsilon(\omega, q)}. \quad (\text{S11})$$

This approximation is justified for the experimentally relevant case of weakly damped CPP,  $q_2 \ll q_1$ . Once  $q_1$  is determined, we can get  $q_2$  using Eq. (1) of the main text:

$$Q^{-1} = \frac{q_2}{q_1} \simeq \frac{\kappa_2(\omega, q_1)}{\kappa_1(\omega, q_1)} + \frac{\text{Im } q_p}{\text{Re } q_p} = \frac{\kappa_2(\omega, q_1)}{\kappa_1(\omega, q_1)} + \frac{\gamma}{\omega}. \quad (\text{S12})$$

This perturbative result follows from Eq. (S10) and is valid assuming both terms on the right-hand side are small.

We also implemented another method for determining the CPP dispersion, which is to look for the maxima of the imaginary part of the total reflection coefficient  $r_p(\omega, q)$ . For the simple case where the encapsulating layer  $j = 1$  is absent, so that  $\kappa_{\text{sup}} = \epsilon_0$ , the equivalence of the two methods can be seen from the formula  $r_p = 1 - 2\kappa_{\text{sub}}(\kappa_{\text{sub}} + \epsilon_0)^{-1}\epsilon^{-1}$  [which follows from Eq. (S6)], implying that a sharp maximum of  $f(\omega, q)$  is also a maximum of  $\text{Im } r_p$ . Note that the imaginary parts of  $\kappa$ ,  $\epsilon$ , and  $r_p$  are all positive if  $\omega$  and  $q > \omega/c$  are real. We verified numerically that in the frequency range of interest, these two methods, both very common, give virtually the

same results. Our calculations were done using `fminbnd` function of Matlab<sup>2</sup>. The results are shown in two figures of the main text: Figure 2c (where the false color background represents  $\text{Im } r_p$ ) and Figure 4b (where the dashed lines are the ridges of the loss function  $f$ ). Additionally, the results obtained for the  $d_2 \rightarrow 0$  limit are shown in Figures S6 and S7. These results are discussed in more detail in Section S1 II below.

The perturbative analysis can also be applied if the doped  $\alpha\text{-RuCl}_3$  layer has a sufficiently small thickness and the corresponding sheet conductivity  $\sigma_s$  is a relatively small correction to the graphene conductivity  $\sigma_g$ . Using Eq. (S9) and (S10), we can obtain the first-order shift  $\delta q$  of the CPP momentum due to  $\sigma_s$  or vice versa,  $\sigma_s$  as a function of  $\delta q$ :

$$\frac{\sigma_s}{\sigma} \approx \frac{\delta q}{q} \left( 1 - \frac{q_p}{\kappa} \frac{\partial \kappa}{\partial q_p} \right). \quad (\text{S13})$$

Let us now turn to the edge CPP. In calculating their dispersion, we relied on the analytical theory presented in Ref. <sup>3</sup>. This theory predicts that the edge excitations show up as the poles of a certain function  $g(\omega, q)$  defined by

$$g(\omega, q) = \tanh I, \quad I = \frac{1}{\pi} \int_0^{\pi} \frac{d\xi}{1 + \xi^2} \ln \epsilon \left( \sqrt{1 + \xi^2} q, \omega \right). \quad (\text{S14})$$

This function seems to be a one-dimensional analog of the response functions  $f$  and  $r_p$  we used to analyze the CPP. However, according to our numerical simulations, neither real nor imaginary part of  $g$  has a definite sign, unlike  $\text{Re } f$  or  $\text{Im } r_p$ . Therefore, we adopted the prescription that the real part of the edge CPP momentum  $q_e$  coincides with the maximum of the *absolute value* of  $g(\omega, q)$ . To find such a maximum, we used the same Matlab function as before. The results are shown in Figure 4b of the main text (solid lines).

For a qualitative understanding of the computed edge CPP spectra, two analytical results are useful. First, as explained above, the effective permittivity  $\kappa$  approaches constant values in the limit of both small and large  $q$ . In this limit, the edge and CPP momenta are connected by a simple rule: the former is  $A = 1.217$  times larger than the latter<sup>3</sup>. This “universal” relation can be derived by noticing that the poles of  $g$  correspond to  $I = i\pi/2$ , which entails an alternative form of the edge CPP dispersion equation (obtained after the substitution  $\xi = q \cot t$ ):

$$\int_0^{\pi/2} dt \ln \left[ -\epsilon \left( \frac{q_e}{\sin t}, \omega \right) \right] = \int_0^{\pi/2} dt \ln \left[ \frac{k}{q_p(\omega)\kappa(\omega, k)} - 1 \right] \Bigg|_{k=\frac{q_e}{\sin t}} = 0. \quad (\text{S15})$$

If  $\kappa$  is momentum-independent, this equation is easy to solve numerically to obtain the quoted result  $q_e = Aq_s$ . However, in our case  $\kappa$  is not constant, primarily because of the presence of the  $h\text{BN}$  overlayer. As a result, the edge-to-surface CPP momentum ratio for the computed dispersions is typically larger than 1.217, sometimes as high as 1.6 (see Figure 4b). The fact that a few-nm thick layer of  $h\text{BN}$  has such a strong effect on edge CPPs indicates that the edge CPP has a substantial contribution of high-momenta Fourier harmonics whose electric field is confined inside  $h\text{BN}$ . The second analytical result concerns the 2D sheet model of the doped  $\alpha\text{-RuCl}_3$  layer. From a perturbative analysis of Eq. (S15) we obtained the following counterpart of Eq. (S13):

$$\begin{aligned}
\frac{\sigma_s}{\sigma} &\approx \frac{\delta q_e}{q_e} \left( 1 - \frac{q_p}{\kappa} \frac{\partial \kappa}{\partial q_p} \right), \\
\overline{z(q)} &\equiv \frac{\int_q^\infty w(q, k) z(k) dk}{\int_q^\infty w(q, k) dk}, \\
w(q, k) &= \frac{1}{\sqrt{k^2 - q^2}} \frac{1}{k - \kappa q_p}.
\end{aligned} \tag{S16}$$

In words, the coefficient for the fractional shift of the edge CPP momentum is given by the average of the logarithmic derivative of  $\kappa$ , weighted with the function  $w(q, k)$ . This weighting function can be thought of as the relative contribution of different Fourier harmonics to the total real-space waveform of the edge CPP excitation.

In the next Section we discuss numerical simulations and fits based on the equations presented in this Section.

## II. Least-squares optimization of the chemical potential

Since the magnitude of charge transfer between the graphene and  $\alpha$ -RuCl<sub>3</sub> layers was unknown, the chemical potential of graphene was made a free parameter in a least-squares fit to the measured CPP dispersions. The objective function  $\chi^2$  to minimize is the residual squared difference between experimental and model plasmon momenta weighted by the observation uncertainties:

$$\chi^2 = \sum_{i=1}^{N_\omega} \frac{(q_{s,i} - q_{s,i}^{obs})^2}{\sigma_{obs,i}^2} \tag{S17}$$

where  $q_s^{obs}$  and  $\sigma_{obs}^2$  are, respectively, the mean and variance of the observed plasmon momenta, and  $N_\omega$  is the number of experiments at different laser frequencies. The fitting was done assuming  $d_2 \rightarrow 0$  limit ( $d_3 = 1.9$  nm), with  $\kappa$  computed from Eqs. (S7), (S8), and (S11). When the conductivity of the doped  $\alpha$ -RuCl<sub>3</sub> layer, Eq. (S4), was included in the calculations with the effective mass equal to the vacuum free electron mass, a value of  $|\mu| = 0.56_{-0.04}^{+0.02}$  eV minimized the residual, see Figure S5. We also considered a scenario where this effective mass was infinitely heavy so that the doping-induced modification of the permittivity of  $\alpha$ -RuCl<sub>3</sub> was absent,  $\epsilon_2 - \epsilon_3 = 0$  and  $d_3 = 2.5$  nm. We found that in this case the best fit was  $|\mu| = 0.62_{-0.03}^{+0.03}$  eV, but agreement between the calculated upper polariton branch and the data appeared worse for our choice of parameters, cf. Figures S5a and S5b. The error bars are likelihood-based confidence intervals<sup>4</sup> describing the parameter space within thresholds on the residual. Thresholds are computed by the quantile function of a chi-squared distribution with a 95% confidence level and 40 degrees of freedom, i.e. the various inputs of the near-field model.<sup>5</sup>

For numerical values of the  $h$ BN and SiO<sub>2</sub> permittivities needed in the calculations, we used the following analytical parametrizations. The in- and out-of-plane responses of  $h$ BN were modeled with a single-oscillator Drude-Lorentz forms

$$\epsilon^a(\omega) = \epsilon_\infty^a + \epsilon_\infty^a \frac{(\omega_{LO}^a)^2 - (\omega_{TO}^a)^2}{(\omega_{TO}^a)^2 - \omega^2 - i\gamma^a \omega} \tag{S18}$$

The permittivity of SiO<sub>2</sub>, which is isotropic, was modeled as the sum of multiple Lorentzians:

$$\epsilon(\omega) = \epsilon_\infty + \sum_i \frac{\Omega_i^2}{\omega_i^2 - \omega^2 - i\gamma_i\omega}. \quad (\text{S19})$$

The permittivity of undoped  $\alpha$ -RuCl<sub>3</sub> was taken from Ref. <sup>6</sup>. As mentioned in Section S1 I, we treated it as isotropic as well. We fitted this permittivity to the sum of three Lorentzians with parameters given in Table S1. The parameters for *h*BN and SiO<sub>2</sub> were taken from Refs. <sup>7,8</sup>. The parameters are summarized in Tables S2 and S3. We then fitted the CPP dispersions using the chemical potential  $\mu$  of graphene as the adjustable parameter, as described above.

$i$	$\omega_i$ (cm <sup>-1</sup> )	$\Omega_i$ (cm <sup>-1</sup> )	$\gamma_i$ (cm <sup>-1</sup> )
1	753.9	2222	941.7
2	276.7	2555	470.7
3	378.4	190.7	101.0

**Table S1: Oscillator parameters for  $\alpha$ -RuCl<sub>3</sub> for use in the frequency range  $750 < \omega$  (cm<sup>-1</sup>)  $< 2500$ . The high-frequency permittivity is  $\epsilon_\infty = 6.191$ <sup>6</sup>.**

	$\omega_{\text{TO}}$ (cm <sup>-1</sup> )	$\omega_{\text{LO}}$ (cm <sup>-1</sup> )	$\gamma$ (cm <sup>-1</sup> )	$\epsilon_\infty$
$\epsilon^\perp$	1360	1614	7	4.9
$\epsilon^\parallel$	760	825	2	2.95

**Table S2: Oscillator parameters for *h*BN<sup>7</sup>.**

$i$	$\omega_i$ (cm <sup>-1</sup> )	$\Omega_i$ (cm <sup>-1</sup> )	$\gamma_i$ (cm <sup>-1</sup> )
1	1172	282.8	13
2	1090	538.5	12
3	1060	529.2	5
4	803	200.0	35
5	460	382.1	13
6	544	289.8	164

**Table S3: Oscillator parameters for SiO<sub>2</sub>. The high-frequency permittivity is  $\epsilon_\infty = 1.96$ <sup>8</sup>.**

In summary, fitting the CPP dispersions, i.e.,  $q_1$ , to the data alone is indicative but probably not sufficient for verifying the existence of a modified optical response from charge transfer into interfacial  $\alpha$ -RuCl<sub>3</sub> layers. However, further stronger evidence for the doping of  $\alpha$ -RuCl<sub>3</sub> is found from analyzing  $q_2$  and deduced from the plasmon quality factor  $Q$ , as discussed in Section S2 below.



## S2. Characterizing the graphene/ $\alpha$ -RuCl<sub>3</sub> interfacial optical response from the CPP losses

### I. Graphene phonon contribution to the plasmon scattering rate

As shown in Ref. <sup>9</sup>, in clean graphene such as exfoliated samples encapsulated in hBN, electron-phonon scattering is the major contributions to the CPP damping. The relevant phonons are the two acoustic phonons [transverse (TA) and longitudinal (LA)], the  $A'_1$  optical phonon around  $K$  point and the two optical phonons around  $\Gamma$  point (TO and LO, degenerate at  $\Gamma$ ). Below we summarize the main steps of the calculation presented in Ref. <sup>9</sup>. The starting point is the formula  $P = 2\sigma_1(\omega)|E|^2$  for the power dissipation in the presence of an oscillating electric field  $E e^{-i\omega t} + c. c.$  It implies that the scattering rate can be computed as

$$\gamma(\omega) = \omega \frac{\sigma_1}{\sigma_2} = \frac{\pi \omega^2}{2 D_g} \frac{P}{|E|^2} \quad (\text{S20})$$

assuming  $\gamma \ll \omega$ . The power dissipation can be found from the Fermi's golden rule<sup>9</sup>:

$$\begin{aligned} P = 2\pi\omega \left| \frac{eE}{\omega} \right|^2 \int \frac{Nd^2k}{(2\pi)^2} \frac{d^2k}{(2\pi)^2} \sum_{\zeta, \zeta_\gamma} \sum_{S, S'} \sum_{v=l, t} \zeta \zeta_\gamma f(\varepsilon_{Sk}) [1 - f(\varepsilon_{S'k'})] \\ \times [n_B(\zeta \hbar \omega_{vq}) + 1] \delta(\varepsilon_{S'k'} - \varepsilon_{Sk} + \zeta \hbar \omega_{vq} - \zeta_\gamma \hbar \omega) \\ \times \left[ \sum_{S''} \frac{W_{S'k'; S''k}^v u_{S''k; Sk}^x}{\varepsilon_{Sk} - \varepsilon_{S''k} + \zeta_\gamma \hbar \omega} - \frac{u_{S'k'; S''k'}^x W_{S''k'; Sk}^v}{\varepsilon_{S'k'} - \varepsilon_{S''k'} + \zeta_\gamma \hbar \omega} \right]^2 \end{aligned} \quad (\text{S21})$$

where  $W_{S'k'; Sk}^v$  is the electron-phonon couple matrix element between the states  $(S', k')$  and  $(S, k)$ ,  $f(\varepsilon)$  is the Fermi occupation number at energy  $\varepsilon$  and  $n_B$  is the phonon occupation number. The transition matrix element due to LA/TA phonons is

$$W^v = i\beta_A \sqrt{\frac{\hbar q^2}{\mu_S \omega_{vq}}} \begin{pmatrix} 0 & i \\ -i & 0 \end{pmatrix} \quad (\text{S22})$$

in the pseudospin basis. It induces the scattering rate

$$\gamma_A(\omega) = \left( 1 + \frac{1}{12} \frac{\omega^2}{\mu^2} \right) \gamma(0) = \left( 1 + \frac{1}{12} \frac{\omega^2}{\mu^2} \right) \frac{1}{\hbar^3} \frac{\beta_A^2 |\mu|}{\mu_S v_F^2} \left( \frac{1}{v_l^2} + \frac{1}{v_t^2} \right) T \quad (\text{S23})$$

In deriving this formula, we assumed  $\omega/\mu$  is a small parameter and kept terms up to the order  $O(\omega^2/\mu^2)$ . The electron-phonon coupling constant  $\beta_A = 5.0 eV$  can be found in Refs. <sup>9</sup> or <sup>10</sup>. The lattice mass density is  $\mu_S = 7.6 \times 10^{-8} g/cm^2$  and the phonon velocities are  $v_l = 2.2 \times 10^6 cm/s$ ,  $v_t = 1.4 \times 10^6 cm/s$ . Equation (S22) indicates that the frequency dependence of  $\gamma_A$  is weak as long as  $\omega < \mu$ .

The transition matrix elements for the  $A'_1$  phonon is

$$W^K = i\beta_K \sqrt{\frac{2\hbar}{\mu_S \omega_K}} \begin{pmatrix} 0 & i \\ -i & 0 \end{pmatrix}, \quad (\text{S24})$$

where  $\beta_K = 14 eV/\text{\AA}$  and  $\omega_K = 1200 cm^{-1}$ . The dominant process is the intra-band emission of the optical phonons. The corresponding scattering rate is

$$\begin{aligned} \gamma_K(\omega) = \frac{3}{2} \frac{\beta_K^2 \mu^2}{\mu_S \omega_K \omega v_F^2} \sum_{\zeta, \zeta_\gamma} \zeta \zeta_\gamma \int_0^\infty dx x \left( x - \zeta \frac{\omega_K}{\mu} + \zeta_\gamma \frac{\omega}{\mu} \right) f(\mu x) \\ \times [1 - f(\mu x - \zeta \omega_K + \zeta_\gamma \omega)] [1 + n_B(\zeta \omega_K)] \end{aligned} \quad (\text{S25})$$

where  $\zeta, \zeta_\gamma$  take values of  $\pm 1$ . At zero temperature, considering photon (not phonon!) absorption only, this expression simplifies to

$$\begin{aligned}\gamma_K(\omega) &= \frac{3}{2} \frac{\beta_K^2 \mu^2}{\mu_S \omega_K \omega v_F^2} \Theta(\omega - \omega_K) \int_{1 - \frac{\omega - \omega_K}{\mu}}^1 dx x \left( x + \frac{\omega - \omega_K}{\mu} \right) \\ &= \frac{3}{2} \frac{\beta_K^2 \mu}{\mu_S \omega_K v_F^2} \Theta(\omega - \omega_K) \frac{\mu}{\omega} \left[ \frac{\omega - \omega_K}{\mu} - \frac{1}{6} \left( \frac{\omega - \omega_K}{\mu} \right)^3 \right]\end{aligned}\quad (\text{S26})$$

Next, the combined scattering of TO and LO phonons results in an isotropic matrix element proportional to  $\beta_\Gamma$ . The intraband emissions of the TO/LO optical phonons contribute to the scattering rate and are the same as Eq. (S25) but with  $\frac{3}{2} \rightarrow 1$  and  $\beta_K, \omega_K$  replaced by  $\beta_\Gamma = 11.4 \text{ eV/\AA}, \omega_\Gamma = 1600 \text{ cm}^{-1}$ . At zero temperature, it simplifies to Eq. (S26), with the same replacement. Altogether, the phonon contribution to the scattering rate of graphene is

$$\gamma_g(\omega) = \gamma_A(\omega) + \gamma_K(\omega) + \gamma_\Gamma(\omega). \quad (\text{S27})$$

The values of the coupling constants can be found in Refs. <sup>9</sup> or <sup>10</sup>.

## II. Extracted optical conductivity of doped $\alpha\text{-RuCl}_3$

To simplify the analysis, we again treat the doped part of  $\alpha\text{-RuCl}_3$  as two-dimensional,  $d_2 \rightarrow 0$ . In this case the scattering rate  $\gamma_{\text{eff}}$  is used in place of  $\gamma$  in Eq. (S12), and should be defined in terms of the total sheet conductivity  $\sigma = \sigma_g + \sigma_s$ . Its relation to the CPP  $Q$  factor  $Q = q_1/q_2$  is as follows:

$$\gamma_{\text{eff}}(\omega) \equiv \omega \frac{\text{Re } \sigma(\omega)}{\text{Im } \sigma(\omega)} = \omega \left[ \frac{1}{Q} - \frac{\kappa_2(\omega, q_1)}{\kappa_1(\omega, q_1)} \right], \quad (\text{S28})$$

where  $\kappa = \kappa_1 + i\kappa_2$  is to be computed from Eqs. (S7), (S8), and (S11). After subtracting the contribution from the substrate, the measured effective frequency dependent scattering rate,  $\gamma_{\text{eff}}$ , is shown in Figures 4b and S9. If both graphene and  $\alpha\text{-RuCl}_3$  are described by Drude models with frequency dependent scattering rates, Eqs. (S1) and (S4) then become

$$\sigma(\omega) = \frac{i D_g}{\pi \omega + i\gamma_g(\omega)} + \frac{i D_s}{\pi \omega + i\gamma_s(\omega)}, \quad (\text{S29})$$

and the effective scattering rate becomes

$$\gamma_{\text{eff}}(\omega) \approx \frac{D_g}{D_g + D_s} \frac{\omega^2 \gamma_g(\omega)}{\omega^2 + \gamma_g^2(\omega)} + \frac{D_s}{D_g + D_s} \frac{\omega^2 \gamma_s(\omega)}{\omega^2 + \gamma_s^2(\omega)} \quad (\text{S30})$$

From Eq. (S10), given the measured plasmon dispersion and damping, the optical conductivity of  $\alpha\text{-RuCl}_3$  can be extracted as

$$\sigma_s(\omega) = i\kappa(\omega, q) \frac{\omega}{2\pi q} - \sigma_g(\omega) \quad (\text{S31})$$

Note that  $q = q_1 + iq_2$  is the complex plasmon momentum while  $\omega$  is a real number. It appears that the major effect of the doped  $\alpha\text{-RuCl}_3$  layer is to bring extra damping to the CPP rather than to shift their dispersion. Thus, the estimation of  $\gamma_g$  from Eq. (S27) shows that more than half of the total measured CPP losses can be due to the proximity to  $\alpha\text{-RuCl}_3$ . As can be seen from

Figure 4c, a typical magnitude of the real part of optical conductivity is  $\text{Re } \sigma_s \approx 0.5 e^2/h \approx 0.08 e^2/\hbar$ . We estimate the relative uncertainty of the extracted  $\text{Re } \sigma_s$  to be about 20%. However, it may contain a systematic error if our estimate of  $\kappa$  or the theoretical scattering rate in graphene is inaccurate, see Sec. S1 II. Nevertheless, the extraction of  $\text{Re } \sigma_s$  is more reliable than the extraction of  $\text{Im } \sigma_s$  or the Drude weight  $D_s$ .

Provided the measurement frequencies are not in the Drude tail  $\omega < \gamma_s$ , which seems likely, having such a low  $\text{Re } \sigma_s$  implies that the mean free path of carriers in  $\alpha$ -RuCl<sub>3</sub> is much smaller than the interparticle distance. Given the interlayer distance<sup>11</sup>  $c = 0.57$  nm, the upper bound on the equivalent bulk conductivity is  $\text{Re } \sigma_{3D} = \text{Re } \sigma_s/c \approx 340 (\Omega \text{ cm})^{-1}$ . In comparison, a weakly-doped cuprate La<sub>1.97</sub>Sr<sub>0.03</sub>CuO<sub>4</sub> (LSCO) has a conductivity<sup>12</sup> of  $200 (\Omega \text{ cm})^{-1}$  in the in-plane direction. It corresponds to the 2D conductivity of  $\sigma_{\text{LSCO}} \approx 0.1 e^2/\hbar$  per atomic layer considering the interlayer distance<sup>13</sup> of 1.32 nm.

Despite the shortness of the mean-free path, we can formally compare our findings for  $\gamma_s(\omega)$  to the predictions of the Fermi liquid theory. The equation

$$\gamma_s(\omega) = [(k_B T)^2 + 0.18(\hbar\omega)^2] / \hbar E_F \quad (\text{S32})$$

where  $E_F = 63$  meV plugged into Eq. (S30) gives the blue curves in Figures S9 and 4a,b,f in the main text. From the comparison in Figure 4b of the main text, the experimental scattering rate  $\gamma_s(\omega, T)$  of  $\alpha$ -RuCl<sub>3</sub> increases with frequency faster than frequency squared. This is different from the behavior typically found in cuprates, where the scattering rate is linear in frequency and temperature.

### S3. Modeling near-field signal from plasmon reflection at a point defect

We assumed that a defect in the graphene- $\alpha$ -RuCl<sub>3</sub> heterostructure caused a local perturbation of the total sheet conductivity  $\sigma = \sigma_g + \sigma_s$  with respect to the asymptotic value  $\sigma(\infty)$ . We denote  $\bar{\sigma}(\mathbf{r}) = \sigma(\mathbf{r})/\sigma(\infty)$  the corresponding relative change. To model the position-dependent near-field signal associated with reflections of CPP from the defect, we considered the integro-differential equation for the scalar potential  $\phi_s$  generated in response to the potential  $\phi_{\text{probe}}$  of a probe<sup>14</sup>:

$$\left[ 1 + \frac{1}{2\pi q_s} V * \nabla \cdot \bar{\sigma}(\mathbf{r}) \nabla \right] \phi(\mathbf{r}) = \phi_{\text{probe}}(\mathbf{r}), \quad \phi = \phi_{\text{probe}} + \phi_s. \quad (\text{S33})$$

Here  $q_s$  is the momentum of the CPP away from the defect [Eq. (S14)],  $V(r) = 1/r$  is the Coulomb kernel, and the asterisk (\*) denotes the spatial convolution over the in-plane coordinate  $\mathbf{r} = (x, y)$ . As an example, we chose  $\bar{\sigma}(\mathbf{r}) \equiv 1 + \delta\Lambda(r/w)$ , where  $\delta$  is the characteristic magnitude of the conductivity fluctuation at the defect,  $w$  is its width, and  $\Lambda(z) = 1/(1+z^2)$  is a Lorentzian function of unit width and height. We solved Eq. (S33) through expansion in an orthonormal basis of plane waves  $\phi_j = A_j e^{i\mathbf{q}_j \cdot \mathbf{r}}$  periodic in a 2D square cell  $x, y \in [-L/2, L/2]$ , with  $A_j$  a normalization constant. If we assemble the Fourier momenta  $\mathbf{q}_j$  and the Fourier coefficients  $\tilde{\phi}_j = \langle \phi_j | \phi \rangle \equiv \int \phi_j^*(\mathbf{r}) \phi(\mathbf{r}) d^2r$  into column vectors  $\vec{q}$  and  $\vec{\phi}$ , respectively, these vectors must obey the equation

$$\vec{\phi} = [q_s - (\delta\vec{Q} + \text{diag } |\vec{q}|)]^{-1} q_s \vec{\phi}_{\text{probe}}, \quad (\text{S34})$$

where  $\vec{Q}$  is the scattering matrix with the elements

$$Q_{ij} = (\hat{\mathbf{q}}_i \cdot \mathbf{q}_j) \left\langle \phi_i \left| \Lambda \left( \frac{r}{w} \right) \right| \phi_j \right\rangle. \quad (\text{S35})$$

We defined another matrix-valued function  $\vec{G}$  by  $\vec{\phi}_s = \vec{G} \vec{\phi}_{\text{probe}}$ . From Eq. (S33), we obtain

$$G_{ij} = \left\langle \phi_i \left| [q_0 - (\delta \vec{Q} + \text{diag } |\vec{q}|)]^{-1} (\delta \vec{Q} + \text{diag } |\vec{q}|) \right| \phi_j \right\rangle. \quad (\text{S36})$$

For translationally invariant system,  $\delta = 0$ , where the momentum is conserved, only the diagonal matrix elements are nonzero. They can be understood as ‘‘in-plane’’ reflection coefficients. The connection to the conventional Fresnel coefficients  $r_p(\omega, q)$  and the graphene loss function  $f(\omega, q)$  discussed in Section S1 is as follows:  $-G_{jj} = 1 - \epsilon(\omega, \mathbf{q}_j)^{-1}$  where  $\epsilon(\omega, \mathbf{q})$  is the effective dielectric function of graphene [Eq. (S9)]. Therefore,  $\text{Im}(-G_{jj}) = f(\omega, \mathbf{q}_j)$  has maxima at the same momenta  $|\mathbf{q}_j| = \text{Re } q_s$  as  $f$  and  $\text{Im } r_p$ . Previous theoretical work has shown that the Fresnel reflection coefficient  $r_p(\omega, q_{\text{probe}})$  is representative of the near-field signal for homogeneous graphene. Here  $q_{\text{probe}}$  is of the order of the inverse curvature radius of the sharp tip of the probe. Motivated by this, we defined the generalized reflection coefficient associated with our spatially localized probe excitation,

$$R \equiv -\vec{\phi}_{\text{probe}}^T \vec{G} \vec{\phi}_{\text{probe}}. \quad (\text{S37})$$

We expect that  $R$  should be representative of the local near-field signal produced by a general inhomogeneous system.

We developed a Python-language computer code implementing the above equations taking advantage of public-domain libraries and we used it to carry out a series of numerical simulations. For simplicity, we approximated  $\phi_{\text{probe}}(\mathbf{r})$  by a potential of a point dipole placed a small distance away from graphene<sup>15</sup>. Given an in-plane probe position  $\mathbf{r}_{\text{probe}}$ , the relative strength  $\delta$  of the perturbation due to the defect, and the defect width  $w$ , the code computes the absolute value of  $R$ . We varied parameters  $\delta$  and  $w$  to achieve maps of  $|R(\mathbf{r}_{\text{probe}})|$  resembling our experimental data. The results are presented in Figure 3 of the main text. Our simulations are consistent with the defect width of  $w \sim 40$  nm, which is comparable to what was found in the AFM topography studies. The leading negative fringe of the radial near-field profiles indicates the depletion of the local conductivity,  $\delta < 0$ . To match the amplitude of this fringe ( $\sim 10\%$ ), the depletion has to be significant,  $|\delta| \sim 1$ .

Our computational method may be suitable for qualitative and quantitative modeling of the near-field response of other spatially inhomogeneous 2D heterostructures. Such applications and details of their implementation will be reported elsewhere.

#### S4. Ab Initio Calculations of Graphene/ $\alpha$ -RuCl<sub>3</sub> Heterostructures

The calculations were performed within the Vienna Ab initio Simulation Package (VASP)<sup>16</sup> using a projector-augmented wave (PAW) pseudopotential in conjunction with the Perdew–Burke–Ernzerhof (PBE)<sup>17</sup> functionals and plane-wave basis set with energy cutoff at 400 eV. For the heterostructures with graphene and monolayer  $\alpha$ -RuCl<sub>3</sub>, we used a hexagonal supercell containing 82 atoms (composed of a  $5 \times 5$  graphene supercell and  $\sqrt{3} \times \sqrt{3}$   $\alpha$ -RuCl<sub>3</sub> supercell). The resulting strain is  $\sim 2.5\%$  for the  $\alpha$ -RuCl<sub>3</sub> monolayer. For graphene on bilayer  $\alpha$ -RuCl<sub>3</sub>, the model consists of 114 atoms. The surface Brillouin zone was sampled by a  $4 \times 4 \times 1$  Monkhorst–Pack k-mesh. A vacuum region of  $\sim 15$  Å was applied. Because of the absence of strong chemical bonding between layers, van der Waals density functional in the opt88 form<sup>18</sup>

was employed for structural optimization. All structures were fully relaxed until the force on each atom was less than  $0.01 \text{ eV \AA}^{-1}$ .

With small Bader charges of 7.01 e (out of 8 e) per orbital, the Ru-4d states cannot be considered fully localized, and therefore, the use of large values of  $U_{4d}$  is understood as an ad hoc fitting parameter without physical basis. Instead, each Chlorine 3p orbital charge is 7.34 e (out of 7 e), indicating the importance to employ correction on both Ru and Cl elements. The evaluation of the Hubbard U terms are computed by employing the generalized Kohn–Sham equations within density functional theory including mean-field interactions (DFT+U), as provided by the Octopus package,<sup>19,20</sup> using the ACBN0<sup>21,22</sup> functional together with the local density approximation (LDA) functional describing the semilocal DFT part. We compute ab initio the Hubbard U and Hund’s J for the 4d orbitals of Ruthenium and 3p orbital of Chlorine. We employ norm-conserving HGH pseudopotentials to get converged effective Hubbard U values (1.96 eV for Ru and 5.31 for Cl) with spin-orbital couplings.

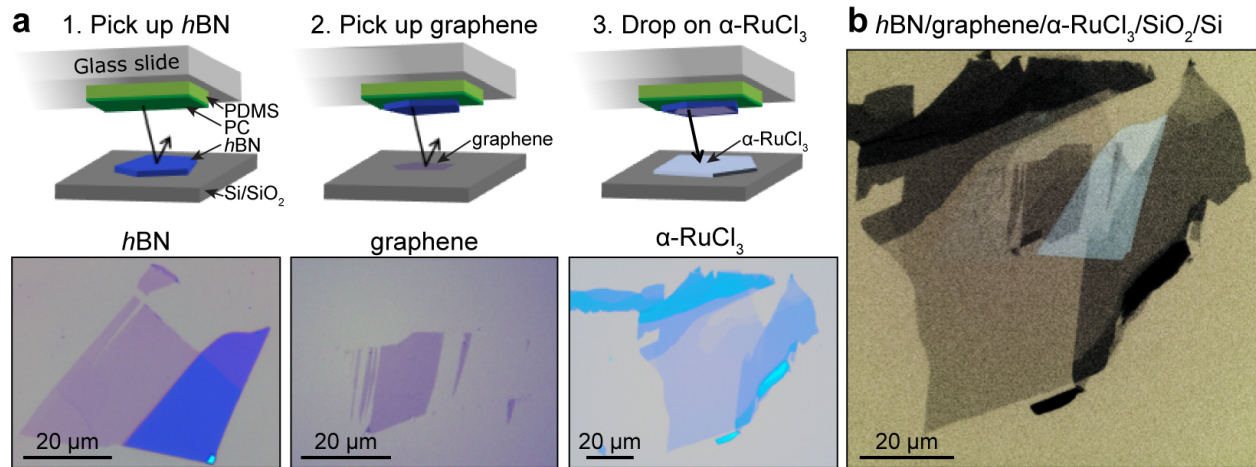


**Figure S1.** Schematic of assembly for  $h\text{BN}/\text{graphene}/\alpha\text{-RuCl}_3/\text{SiO}_2/\text{Si}$ . (a) Schematic of the heterostructure assembly. A polycarbonate (PC) film is used to sequentially pick up  $h\text{BN}$  and graphene, which is finally deposited on exfoliated  $\alpha\text{-RuCl}_3/\text{SiO}_2/\text{Si}$ . (b) Optical image of resulting  $h\text{BN}/\text{graphene}/\alpha\text{-RuCl}_3/\text{SiO}_2/\text{Si}$  heterostructure.

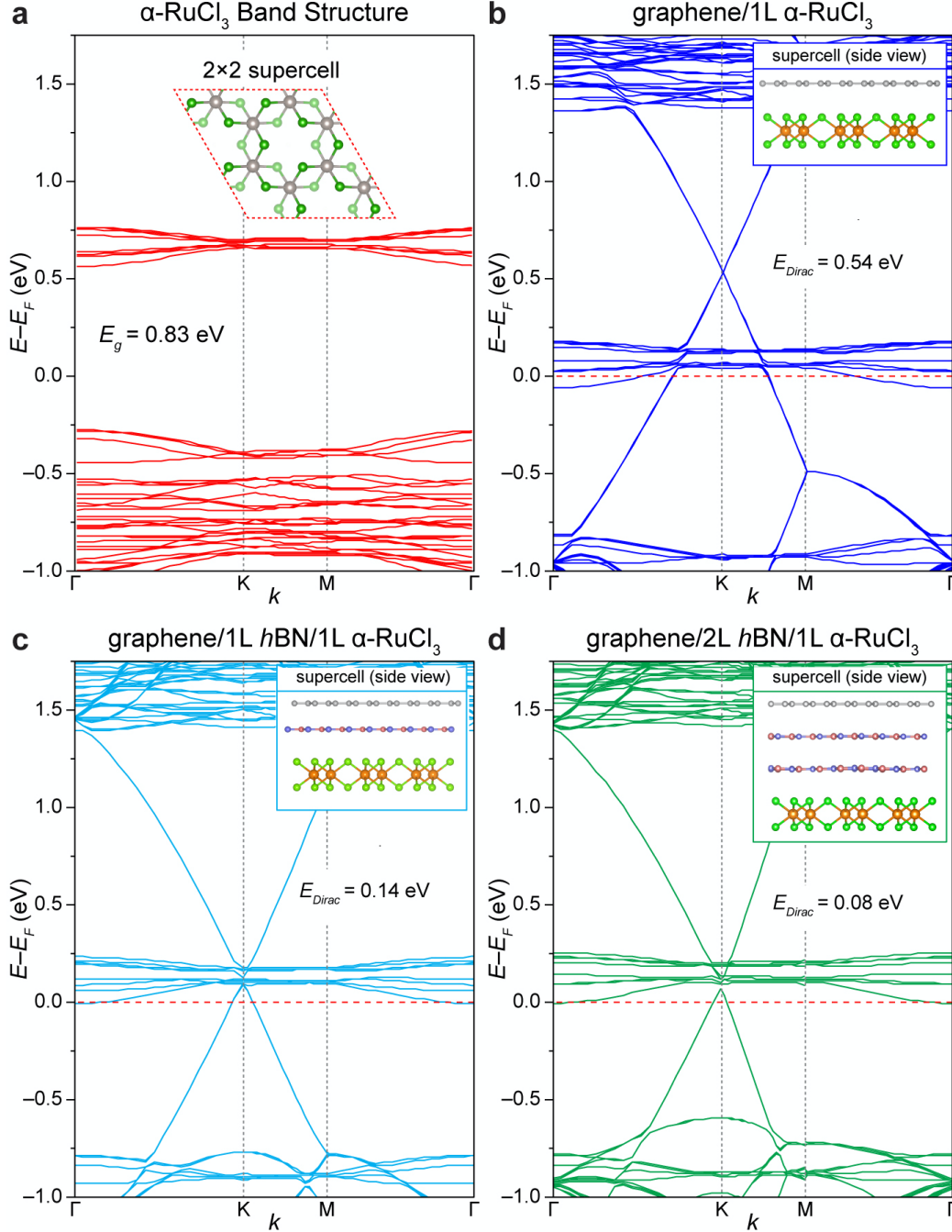


**Figure S2.** Theoretical electronic structure of freestanding  $\alpha$ -RuCl<sub>3</sub> and graphene/ $\alpha$ -RuCl<sub>3</sub> with *h*BN spacers. (a) DFT+U+SOC band structure for 2 $\times$ 2  $\alpha$ -RuCl<sub>3</sub> supercell shown in the inset. Our calculations account for different values of the Hubbard *U* for the Ru 4*d* and Cl 3*p* orbitals ( $U_{4d} = 1.96$  eV and  $U_{3p} = 5.31$  eV, respectively), which allows for an accurate description of its band structure. The bandgap of the  $\alpha$ -RuCl<sub>3</sub> monolayer is 1.07 eV, in excellent agreement with experimental observations (1.2 eV)<sup>23</sup>. (b) Calculated band structure of graphene/ $\alpha$ -RuCl<sub>3</sub> reproduced from Figure 1c. Band structures with (c) one and (d) two *h*BN spacer layers show an incremental shift in the interlayer charge transfer as indicated by the shift in the Dirac point relative to  $E_F$ .

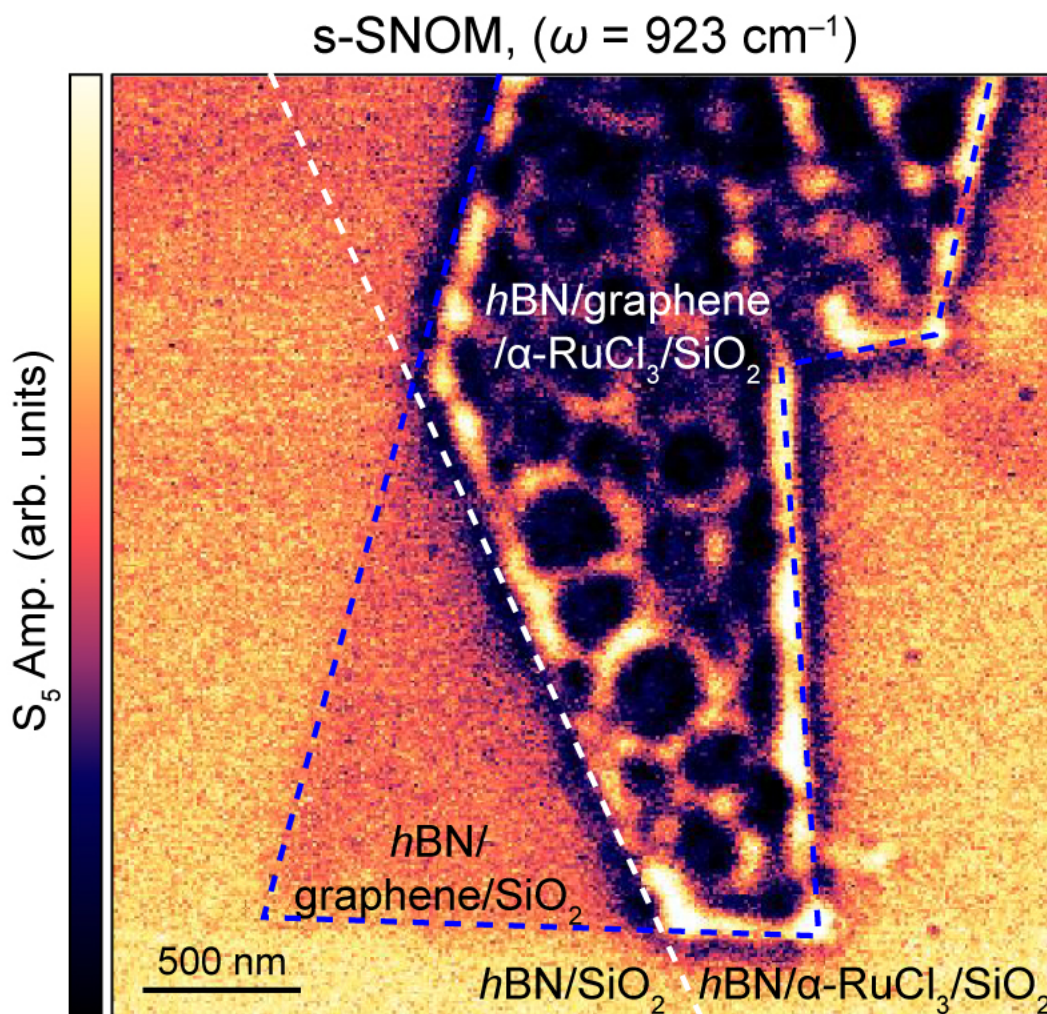


**Figure S3.** Comparison of Near-field Amplitude of  $h\text{BN}/\text{graphene}/\alpha\text{-RuCl}_3/\text{SiO}_2$  vs.  $h\text{BN}/\text{graphene}/\text{SiO}_2$ . s-SNOM image ( $\omega = 923 \text{ cm}^{-1}$ ) of the near-field  $S_5$  amplitude of a piece of graphene that is partially on and off of  $\alpha\text{-RuCl}_3$ . The blue dashed line traces the border of the graphene flake, while the white dashed line traces the edge of  $\alpha\text{-RuCl}_3$  on an  $\text{SiO}_2$  substrate. As is evident from the image, the CPP fringes are only observed for graphene that is in direct contact with  $\alpha\text{-RuCl}_3$ , while the graphene directly on  $\text{SiO}_2$  possesses no such fringes.



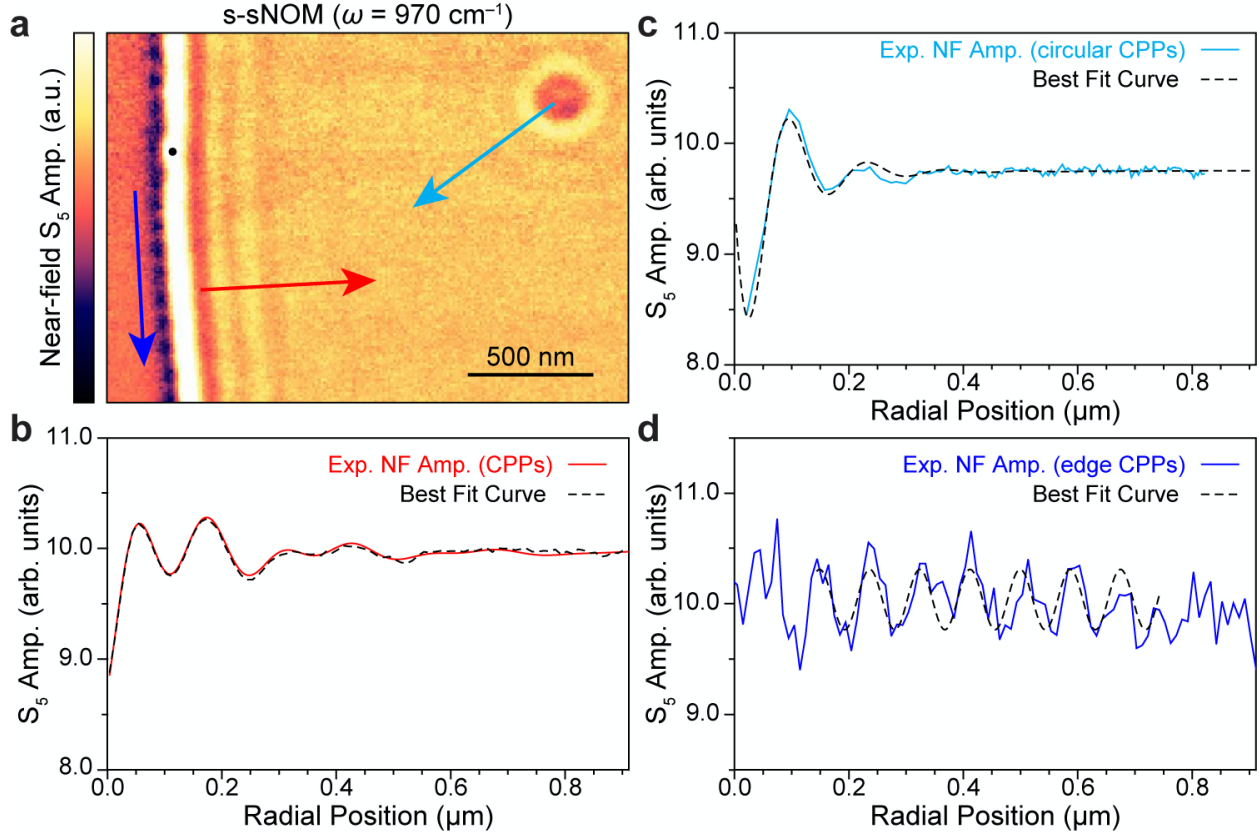


**Figure S4.** Examples fits to the three types of CPP cross-sections. (a) Map of the near-field  $S_5$  amplitude near a graphene edge ( $\omega = 970 \text{ cm}^{-1}$ ) showing CPPs (red arrow), circular CPPs (cyan arrow), and edge CPPs (blue arrow). The solid black circle denotes a notch in the graphene edge that is treated as an edge-plasmon reflector. (b) Red line: the average line profile of the near-field amplitude perpendicular to the graphene edge, as shown in (a). Black dashed line: The best-fit curve to the red line using the ansatz presented in <sup>24</sup>:  $S_0 + A \frac{e^{-i(q_1+iq_2)x}}{R^a+x^a} + BH_0^{(1)}(2(q_1+iq_2)x)$ , where  $S_0$  is the bulk near-field amplitude,  $R$  is the approximate tip radius (25 nm),  $H_0^{(1)}$  is the first Hankel function of order zero, and  $q_1$  and  $q_2$  are the real and imaginary components of the plasmon wave vector, respectively. (c) Cyan line: the average line profile of the near-field amplitude as a function of radial distance from the center of a point defect. Black dashed line: The best-fit curve to the cyan line assuming only cylindrical components (i.e. only constant and Hankel terms of the equation in (b)). (d) Blue line: The average line profile of the near-field amplitude parallel to the graphene edge. Black dashed line: The best fit curve to the blue line using plane-waves. Edge CPP fringes are expected to correspond to  $\lambda_p/2$  standing-waves originating from reflection of tip-launched plasmons from notches in the graphene edge, such as that denoted in (a) with a solid black circle.

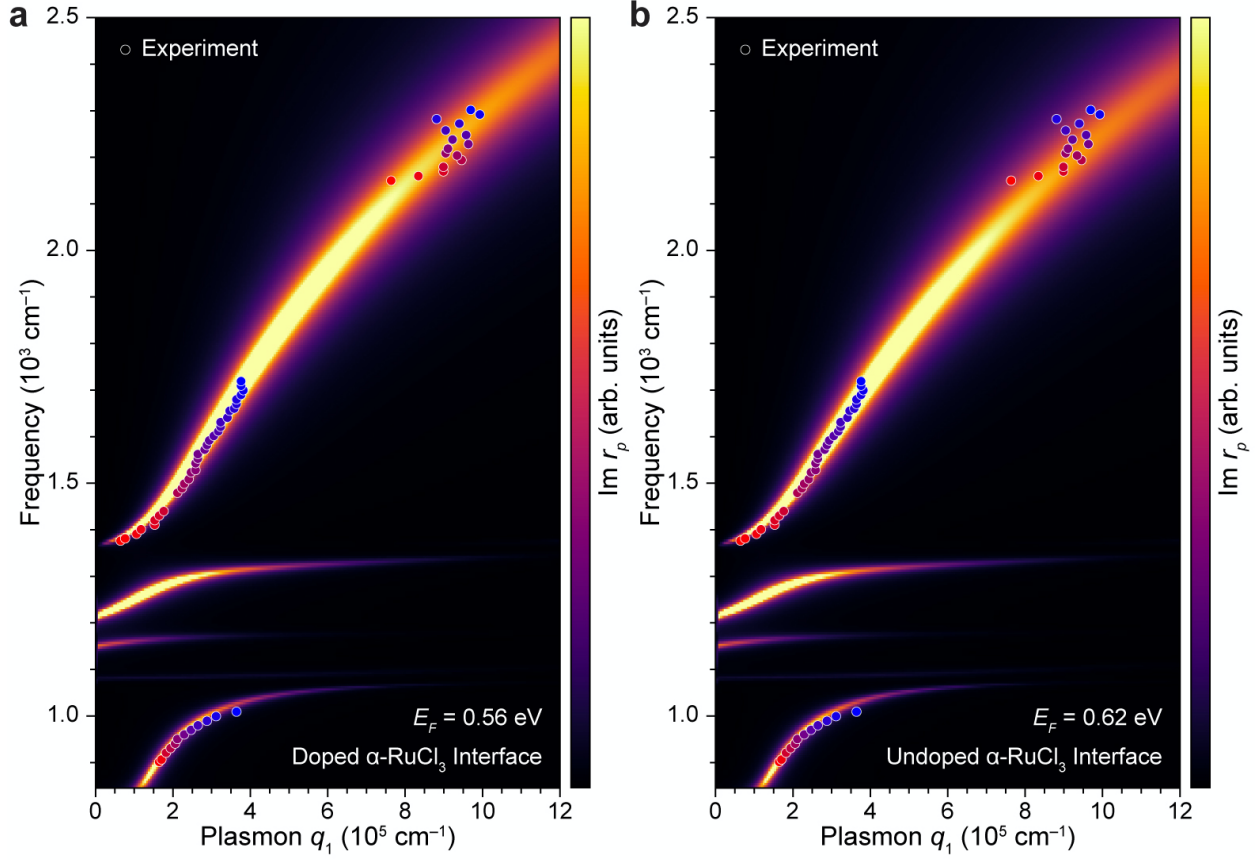


**Figure S5.** Model CPP dispersions of  $h\text{BN}/\text{graphene}/\alpha\text{-RuCl}_3/\text{SiO}_2$  with and without doped interfacial  $\alpha\text{-RuCl}_3$ . The experimental dispersion from Figure 2c of the main text plotted alongside the best-fit  $\text{Im } r_p$  calculations based on the experimental stack shown in Figure S8 assuming (a) doped interfacial  $\alpha\text{-RuCl}_3$  ( $E_F = 0.56$  eV) and (b) undoped interfacial  $\alpha\text{-RuCl}_3$  ( $E_F = 0.62$  eV). While both (a) and (b) capture the essence of the experimental data, (a) has the best goodness-of-fit.

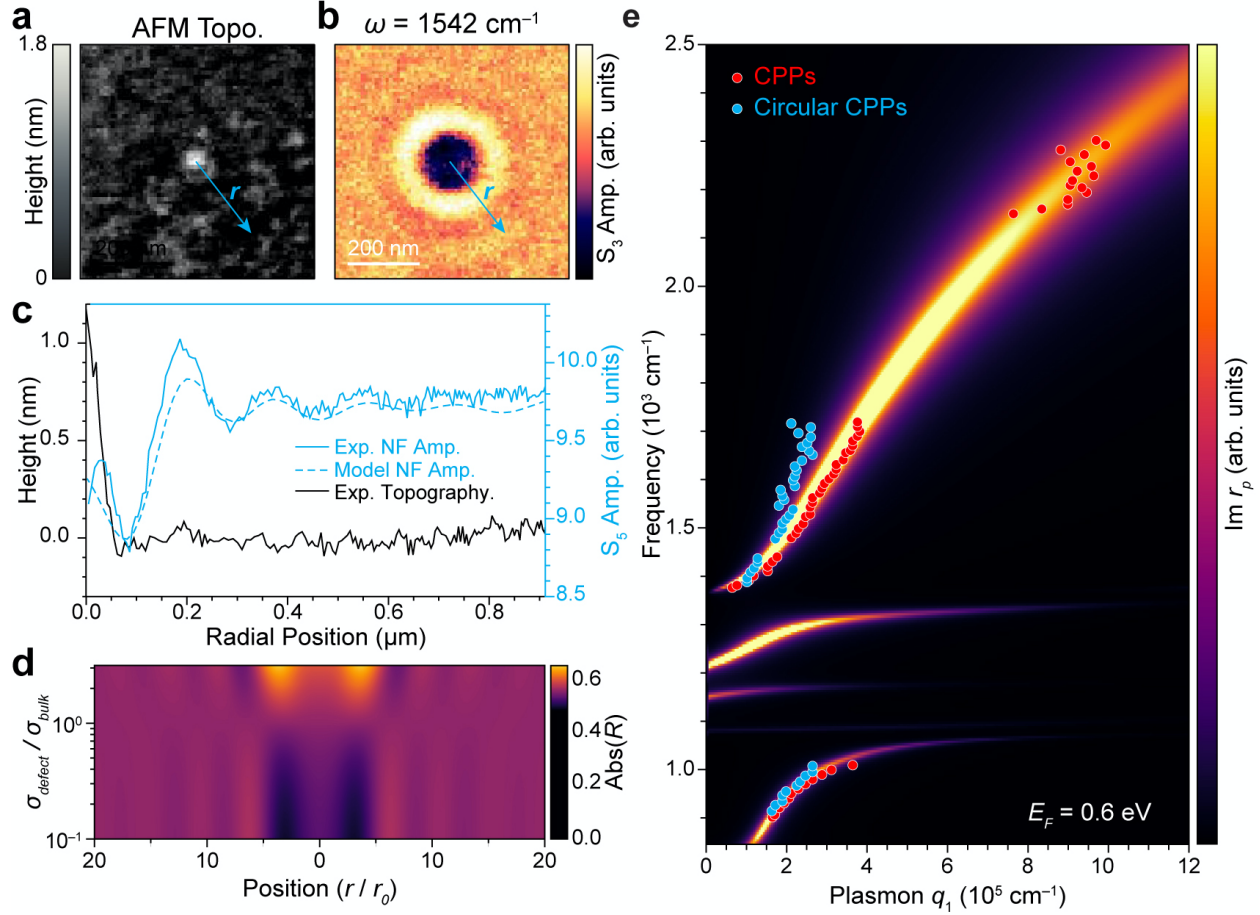


**Figure S6.** Analysis of circular CPP fringes near point defects in graphene/ $\alpha$ -RuCl<sub>3</sub> heterostructures. (a) AFM-topography near a topographic point defect. (b) Map of the near-field amplitude ( $\omega = 1542 \text{ cm}^{-1}$ ) corresponding to the region in (a). (c) Solid cyan curve: Experimental near-field amplitude as a function of radial distance from the topographic point defect for  $\omega = 920 \text{ cm}^{-1}$ . Dashed cyan curve: the model fit to the experimental near-field profile based on the assumption of a Lorentzian charge-deficit with  $r = 40 \text{ nm}$  at  $x = 0$ . Solid black curve: radial line profile of AFM topography as a function of distance from the center of the defect. (d) Model radial fringe profile as a function of defect conductivity  $\sigma_{\text{defect}}$  relative to the graphene bulk. Effective reflectance  $R$  of illuminating fields from a dipole-like probe approximate the experimental near-field signal. The sign and magnitude of the first fringe are determined by the magnitude of the defect conductivity relative to that of the bulk. (e)  $\text{Im } r_p$  and the experimental CPP dispersion (red dots) reproduced from Figure 2c along with the experimental circular CPP dispersion (cyan). While the two experimental dispersions agree well for  $\omega < 1550 \text{ cm}^{-1}$ , CPPs at higher frequencies are pushed to lowered  $q$ , perhaps due to a nearby resonances in draped debris.

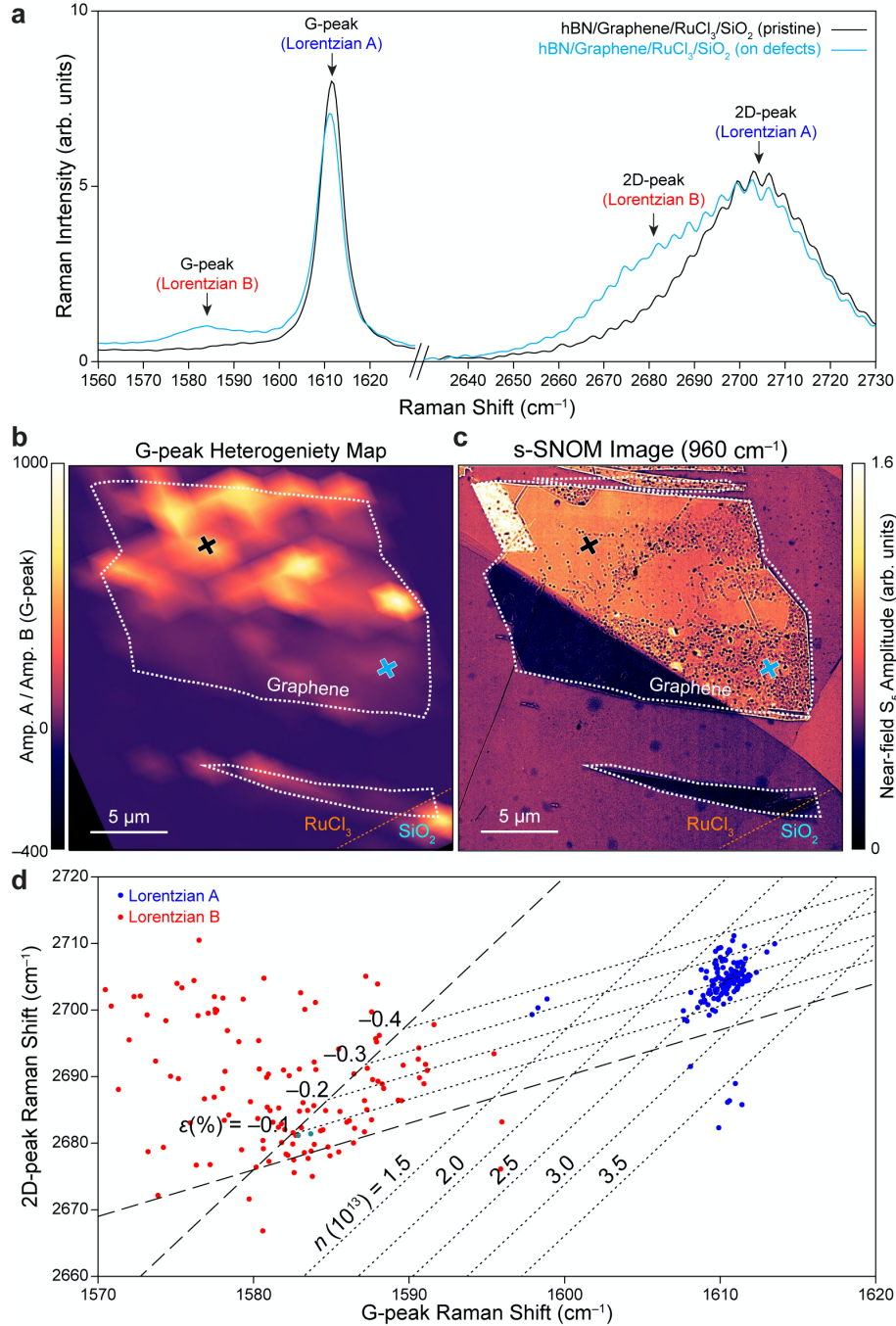


**Figure S7.** Raman analysis of *h*BN/graphene/ $\alpha$ -RuCl<sub>3</sub>/SiO<sub>2</sub>. (a) Raman spectra conducted on graphene with low (black line) and high (cyan line) point defect density. All spectra show a stiffened G and 2D peak (Lorentzian A), and areas with high defect density show additional unshifted G and 2D peaks (Lorentzian B). (b) Spatial dependence of the G-peak heterogeneity showing the ratio of the amplitudes of Lorentzian A to Lorentzian B as defined in (a). (c) Map of the near-field S<sub>5</sub> amplitude over the same region of graphene shown in (b). Areas that show a relative high amplitude for Lorentzian A have a low defect density, while the opposite is true for areas with a high defect density. (d) Plot of the experimental 2D versus G peak Raman shifts shows the co-existence of a uniformly strained, doped phase (blue dots, Lorentzian A), and randomly strained, undoped phase (red dots, Lorentzian B).

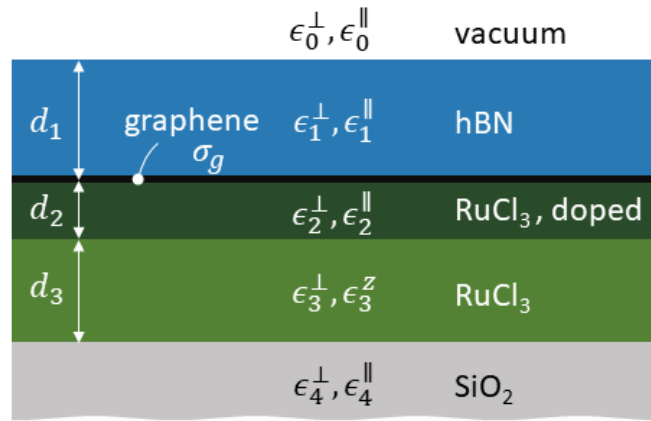


**Figure S8.** Schematic of the *h*BN/graphene/ $\alpha$ -RuCl<sub>3</sub>/SiO<sub>2</sub>/Si heterostructure.

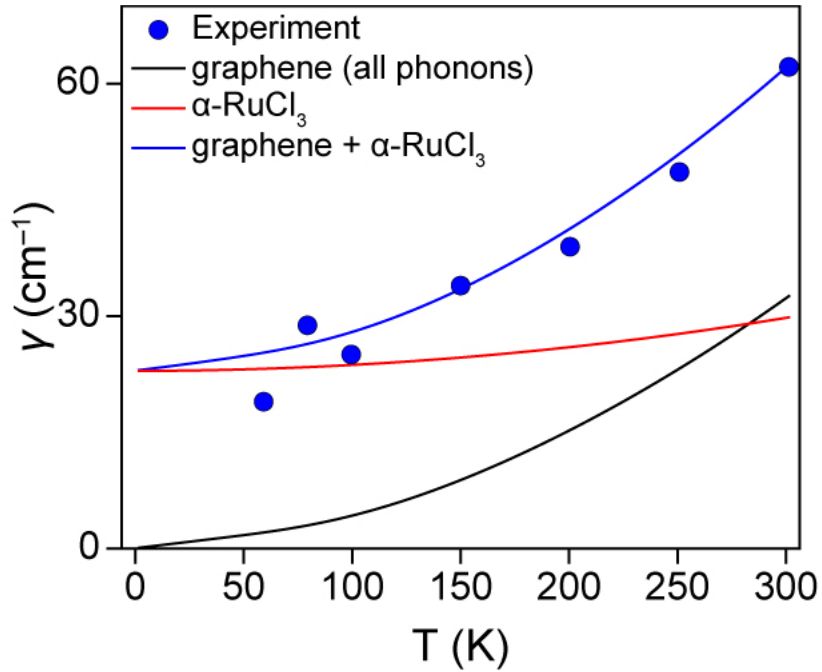


**Figure S9.** Temperature-dependent scattering in graphene/ $\alpha$ -RuCl<sub>3</sub>. Blue dots: The extracted scattering rate versus temperature derived from the quality factor in Figure 4f of the main text with dielectric losses subtracted. Black line: The model temperature-dependent scattering rate based on graphene phonons only. Red Line: The temperature-dependent contribution of the model interfacial  $\alpha$ -RuCl<sub>3</sub> layer to the effective scattering rate. Blue line: The total temperature-dependent scattering rate of the graphene and interfacial  $\alpha$ -RuCl<sub>3</sub> layer.

## References

- 1 Wu, J.-S.; Basov, D. N. & Fogler, M. M. Topological insulators are tunable waveguides for hyperbolic polaritons. *Physical Review B* **2015**, *92*, 205430
- 2 MATLAB (The MathWorks Inc, Natick, Massachusetts, 2019).
- 3 Volkov, V. & Mikhailov, S. A. Edge magnetoplasmons: low frequency weakly damped excitations in inhomogeneous two-dimensional electron systems. *Sov. Phys. JETP* **1988**, *67*, 1639-1653
- 4 Meeker, W. Q. & Escobar, L. A. Teaching about approximate confidence regions based on maximum likelihood estimation. *The American Statistician* **1995**, *49*, 48-53
- 5 Ruta, F. L.; Sternbach, A. J.; Dieng, A. B.; McLeod, A. S. & Basov, D. N. Quantitative nano-infrared spectroscopy of anisotropic van der Waals materials. *Nano Letters* **2020**
- 6 Reschke, S.; Mayr, F.; Widmann, S.; Nidda, H.-A.; Tsurkan, V.; Eremin, M.; Do, S.-H.; Choi, K.; Wang, Z. & Loidl, A. Sub-gap optical response in the Kitaev spin-liquid candidate  $\alpha$ - $\text{RuCl}_3$ . *Journal of Physics: Condensed Matter* **2018**, *30*,
- 7 Caldwell, J. D.; Kretinin, A. V.; Chen, Y.; Giannini, V.; Fogler, M. M.; Francescato, Y.; Ellis, C. T.; Tischler, J. G.; Woods, C. R.; Giles, A. J.; Hong, M.; Watanabe, K.; Taniguchi, T.; Maier, S. A. & Novoselov, K. S. Sub-diffractive volume-confined polaritons in the natural hyperbolic material hexagonal boron nitride. *Nature Communications* **2014**, *5*, 5221
- 8 Kučirková, A. & Navrátil, K. Interpretation of infrared transmittance spectra of  $\text{SiO}_2$  thin films. *Applied spectroscopy* **1994**, *48*, 113-120
- 9 Ni, G. X.; McLeod, A. S.; Sun, Z.; Wang, L.; Xiong, L.; Post, K. W.; Sunku, S. S.; Jiang, B. Y.; Hone, J.; Dean, C. R.; Fogler, M. M. & Basov, D. N. Fundamental limits to graphene plasmonics. *Nature* **2018**, *557*, 530-533
- 10 Sohler, T.; Calandra, M.; Park, C.-H.; Bonini, N.; Marzari, N. & Mauri, F. Phonon-limited resistivity of graphene by first-principles calculations: Electron-phonon interactions, strain-induced gauge field, and Boltzmann equation. *Physical Review B* **2014**, *90*, 125414
- 11 Johnson, R. D.; Williams, S. C.; Haghighirad, A. A.; Singleton, J.; Zapf, V.; Manuel, P.; Mazin, I. I.; Li, Y.; Jeschke, H. O.; Valentí, R. & Coldea, R. Monoclinic crystal structure of  $\alpha$ - $\text{RuCl}_3$  and the zigzag antiferromagnetic ground state. *Physical Review B* **2015**, *92*, 235119
- 12 David, B. T.; Young-Duck, Y.; Axel, Z.; Liu, H. L.; Manuel, A. Q.; Moore, S. W.; John, B. G.; Beomhoan, O.; John, T. M.; Ronald, J. K.; Marshall, O. & Cho, J. H. in *Proc.SPIE*.
- 13 Croft, T. P.; Lester, C.; Senn, M. S.; Bombardi, A. & Hayden, S. M. Charge density wave fluctuations in  $\text{La}_{2-x}\text{Sr}_x\text{CuO}_4$  and their competition with superconductivity. *Physical Review B* **2014**, *89*, 224513
- 14 Rejaei, B. & Khavasi, A. Scattering of surface plasmons on graphene by a discontinuity in surface conductivity. *Journal of Optics* **2015**, *17*, 075002
- 15 Nikitin, A. Y.; Alonso-González, P.; Vélez, S.; Mastel, S.; Centeno, A.; Pesquera, A.; Zurutuza, A.; Casanova, F.; Hueso, L. E.; Koppens, F. H. L. & Hillenbrand, R. Real-space mapping of tailored sheet and edge plasmons in graphene nanoresonators. *Nature Photonics* **2016**, *10*, 239-243

- 16 Kresse, G. & Furthmüller, J. Efficient iterative schemes for ab initio total-energy  
calculations using a plane-wave basis set. *Physical Review B* **1996**, *54*, 11169-11186
- 17 Perdew, J. P.; Burke, K. & Ernzerhof, M. Generalized gradient approximation made  
simple. *Physical review letters* **1996**, *77*, 3865
- 18 Klimeš, J.; Bowler, D. R. & Michaelides, A. Van der Waals density functionals applied  
to solids. *Physical Review B* **2011**, *83*, 195131
- 19 Andrade, X.; Strubbe, D.; De Giovannini, U.; Larsen, A.; Oliveira, M.; Alberdi-  
Rodriguez, J.; Varas, A.; Theophilou, I.; Helbig, N.; Verstraete, M.; Stella, L.; Nogueira,  
F.; Aspuru-Guzik, A.; Castro, A.; Marques, M. & Rubio, A. Real-space grids and the  
Octopus code as tools for the development of new simulation approaches for electronic  
systems. *Phys. Chem. Chem. Phys.* **2015**, *17*,
- 20 Tancogne-Dejean, N.; Oliveira, M. J. T.; Andrade, X.; Appel, H.; Borca, C. H.; Le  
Breton, G.; Buchholz, F.; Castro, A.; Corni, S.; Correa, A. A.; De Giovannini, U.;  
Delgado, A.; Eich, F. G.; Flick, J.; Gil, G.; Gomez, A.; Helbig, N.; Hübener, H.; Jestädt,  
R.; Jornet-Somoza, J.; Larsen, A. H.; Lebedeva, I. V.; Lüders, M.; Marques, M. A. L.;  
Ohlmann, S. T.; Pipolo, S.; Rampp, M.; Rozzi, C. A.; Strubbe, D. A.; Sato, S. A.;  
Schäfer, C.; Theophilou, I.; Welden, A. & Rubio, A. Octopus, a computational  
framework for exploring light-driven phenomena and quantum dynamics in extended and  
finite systems. *The Journal of Chemical Physics* **2020**, *152*, 124119
- 21 Tancogne-Dejean, N.; Oliveira, M. J. T. & Rubio, A. Self-consistent DFT+U method for  
real-space time-dependent density functional theory calculations. *Physical Review B*  
**2017**, *96*, 245133
- 22 Agapito, L. A.; Curtarolo, S. & Buongiorno Nardelli, M. Reformulation of DFT+U as a  
Pseudohybrid Hubbard Density Functional for Accelerated Materials Discovery. *Physical  
Review X* **2015**, *5*, 011006
- 23 Banerjee, A.; Bridges, C. A.; Yan, J. Q.; Aczel, A. A.; Li, L.; Stone, M. B.; Granroth, G.  
E.; Lumsden, M. D.; Yiu, Y.; Knolle, J.; Bhattacharjee, S.; Kovrizhin, D. L.; Moessner,  
R.; Tennant, D. A.; Mandrus, D. G. & Nagler, S. E. Proximate Kitaev quantum spin  
liquid behaviour in a honeycomb magnet. *Nature Materials* **2016**, *15*, 733-740
- 24 Woessner, A.; Lundeberg, M. B.; Gao, Y.; Principi, A.; Alonso-González, P.; Carrega,  
M.; Watanabe, K.; Taniguchi, T.; Vignale, G.; Polini, M.; Hone, J.; Hillenbrand, R. &  
Koppens, F. H. L. Highly confined low-loss plasmons in graphene–boron nitride  
heterostructures. *Nature Materials* **2015**, *14*, 421-425